OXFORD JOURNAL
OF STUDENT
SCHOLARSHIP

AI-Assisted LiDAR Mapping and Biometric Telemetry for Real-Time Risk Identification in Underground Exploration

Lizi Shamugia
shamugializi2504@gmail.com

ABSTRACT

This research investigates the efficacy of an integrated risk-focused framework designed for safety assessment in underground systems where GPS (Global Positioning System) and vision-based sensors are unreliable. Traditional exploration often relies on static mapping that fails to account for dynamic hazards and physiological stress. This study proposes a dual-node architecture that fuses wave-based 2D LiDAR (Light Detection and Ranging) mapping with wearable biometric monitoring to provide real-time risk identification. Utilizing an RPLIDAR sensor, the system employs Simultaneous Localization and Mapping to reconstruct 3D environments while identifying spatial risks such as restricted clearance and obstacle density. Due to current hardware deployment stages, the methodology utilizes simulated LiDAR datasets to verify the Artificial intelligence's ability to categorize environmental hazards and provide emergency pathfinding guidance. Results indicate that integrating human health indicators with spatial geometry allows for a more comprehensive safety assessment than geometric mapping alone. This research contributes a scalable, human-centric approach to improving the reliability of search and rescue operations in complex, GPS-denied underground environments.

Index Terms - AI-assisted guidance, Biometric telemetry, LiDAR mapping, Risk identification, SLAM, Underground systems.

INTRODUCTION

Underground cave environments represent one of the most challenging settings for navigation, mapping and safety assessment. The absence of Global Positioning System (GPS) signals, low visibility, irregular geometries, unstable terrain and potential environmental hazards such as toxic gas accumulation create conditions in which traditional vision-based and satellite-based localization systems are unreliable. These limitations significantly increase operational risk for explorers, rescue teams and autonomous robotic platforms. As interest grows in subterranean exploration for geological research, environmental monitoring and emergency response, the development of reliable mapping and risk assessment systems in GPS-denied environments has become an important research priority.

Currently, cave-related risks are primarily managed through preventive measures, such as pre-entry risk assessments and training programs, or through reactive measures like cave rescue organizations. These traditional methods often rely heavily on human judgment, which can be inconsistent in rapidly changing underground environments. Furthermore, many safety assessments occur before or after exploration, leaving a critical gap in real-time safety monitoring during the mission itself. While studies have demonstrated the accuracy of these mapping systems, they typically focus on navigation efficiency or mapping completeness rather than integrated human safety. There is currently limited use of real-time, integrated technological systems that can continuously identify environmental and physiological risks while exploration is ongoing.

This research seeks to bridge the gap between autonomous mapping and active human safety monitoring. The central research question is: *How effectively can integrated environmental sensing, wave-based cave mapping and wearable monitoring systems support risk identification and safety assessment in GPS-denied cave environments?*

The aim of this study is to move beyond the separate goals of mapping accuracy and navigation to create a system that provides integrated safety support. The study hypothesizes that integrating environmental sensing, SLAM-based 3D mapping and wearable monitoring of human health indicators can enable the development of a reliable system that reduces operational strain on underground crews and mitigates the risk of sudden catastrophic failures. This research seeks to infer that an integrated technological approach can more effectively identify and manage risks in real-time compared to traditional, human-reliant methods.

Our research aims to contribute to the existing academic discussion on subterranean exploration and safety systems. To achieve this, it is necessary to review previously published studies and identify opportunities to introduce new approaches or perspectives to already established methods. In this context, several studies have explored technological solutions designed to reduce the workload and risks faced by individuals working in underground environments.

The current academic conversation regarding subterranean robotics is centered on the development of robust Simultaneous Localization and Mapping (SLAM) frameworks. *Grasso et al. (2023)* [1] demonstrated the effectiveness of SLAM and UAV/LiDAR systems in generating detailed 3D point clouds of real cave environments, using terrestrial LiDAR for validation. Building on this, *Sun et al. (2025)* [2] proposed a LiDAR-based SLAM framework with an anti-collision drone design, highlighting how multi-sensor fusion improves localization performance in complex subterranean spaces.

However, extreme underground environments continue to pose significant technical hurdles. *Ebadi et al. (2022)* [3] reviewed the state-of-the-art SLAM strategies, noting that poor visibility and computational constraints remain major open problems. To address these risks safely, *Galea (2025)* [4] utilized virtual 3D testbeds to simulate SLAM techniques, analysing performance metrics such as loop closure and drift in GPS-denied, low-feature conditions.

Despite these advancements, there is a clear knowledge gap: existing research often focuses on sensor performance and mapping accuracy separately from real-world human safety needs. This project intends to offer a new perspective by shifting the focus toward human health-centered data and integrated safety support. By developing a prototype that combines environmental sensing with wearable health monitoring, this research builds upon established mapping work to provide a more comprehensive and responsive safety framework for underground exploration.

METHODOLOGY

This section details the multi-layered system designed to answer the research question regarding integrated risk identification in GPS-denied environments. The research utilizes a dual-prototype approach: an autonomous aerial agent for environmental mapping and a wearable node for physiological monitoring to collect real-time data in controlled, cave-like settings.

This part of the paper explains the technical specifications of the sensors used, the mathematical transformations required for wave-based mapping and the logic behind the integrated risk-scoring engine. By synthesizing spatial data with human-centered health indicators, the methodology demonstrates a shift from simple navigation to a comprehensive, responsive safety framework.

To begin the technical breakdown of the methodology, we first examine the structural assembly of the autonomous mapping agent. This module serves as the primary tool for navigating and sensing the hazardous subterranean environments where traditional tools fail.

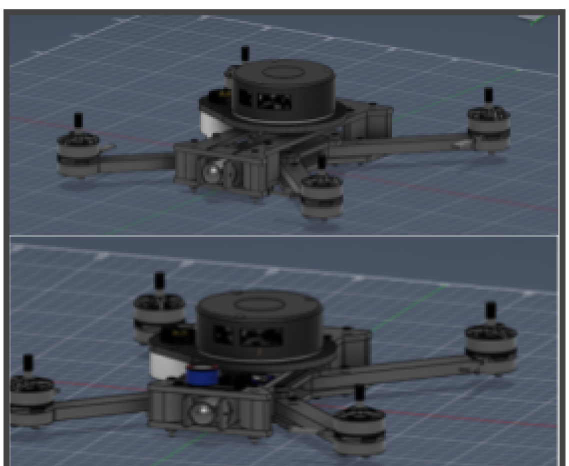

FIGURE I.1 : THE AUTONOMOUS MAPPING AGENT PROTOTYPE (SELF-MADE USING AUTODESK FUSION SOFTWARE)

II.A The Autonomous Mapping Agent (UAV) Prototype

This prototype is a custom-engineered quadcopter designed to carry an integrated sensor suite for real-time risk identification. Consistent with the deployment stage disclosed in the abstract, this design is a CAD-modelled conceptual prototype (self-made using Autodesk Fusion) rather than an assembled and flight-tested unit; the named components below (RPLiDAR A1, MQ-4, MQ-7, MAX30102, MPU6050, ESP32) describe the design-stage sensor selection, not hardware that has been physically integrated and tested to date. As shown in the assembly **figure I.1**, the hardware is organized to maximize the field of view for its primary "wave-based" sensors.

RPLiDAR A1 Integration: The large circular component mounted centrally on top is the **RPLiDAR A1** laser scanner. It is positioned to provide an unobstructed 360-degree horizontal scan, which is essential for creating the 2D and 3D point clouds of the cave's spatial structure.

- **Environmental Sensing Suite**: Mounted at the front and sides of the central frame are specialized modules for atmospheric monitoring. These include:

- **Gas Sensors**: To detect hazardous air quality and oxygen depletion. The system specifically targets **Methane (CH_4)** for explosion prevention, **Carbon Monoxide (CO)** for toxicity monitoring, and **Oxygen (O_2)** concentrations to identify hypoxic zones. Specifically:
    - **Methane (CH_4):** Monitored via the **MQ-4** sensor, calibrated to detect concentrations that could pose an explosive risk.
    - **Carbon Monoxide (CO):** Monitored via the **MQ-7** sensor to detect the presence of toxic 'silent killer' gases.
    - **Oxygen (O_2):** Monitored via an electrochemical oxygen sensor to identify depletion zones (hypoxia) where levels fall below the safe **19.5%** threshold.
    - **Thermal/Temperature Sensors**: To identify abnormal heat zones or fire proximity gradients.

- **Onboard Processing Power**: Hidden within the central chassis is the microprocessor that handles the AI logic and SLAM algorithms. This allows the drone to understand its own position while simultaneously building a map of the unknown environment.

- **Structural Design**: The wide-arm quadcopter configuration provides the flight stability needed to maintain high-resolution sensor data in tight, enclosed spaces.

By mounting these diverse sensors on a single mobile platform, the drone acts as a proactive safety agent that "sees" invisible environmental risks, such as toxic gases or structural blockages before the human explorer reaches them.

II.B The Wearable Biometric Node Prototype

To provide the "human health-centered data" that is often missing from traditional subterranean mapping research, this second hardware module was developed as a wearable synchronization node. As with the mapping agent above, this module is a design-stage conceptual prototype (CAD-modelled in Autodesk Fusion) rather than an assembled and tested device. The device is envisioned as a 3D-printed wristband, designed to sit comfortably on an explorer's arm while maintaining direct contact for biological sensing.

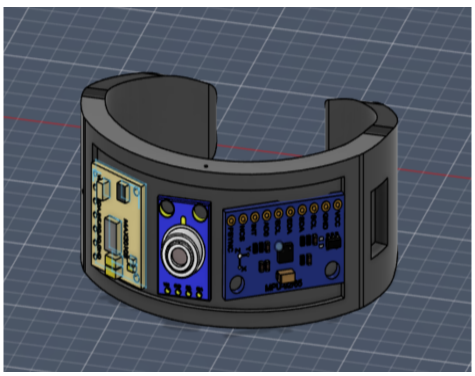

figure II: the wearable biometric node
(self-made using autodesk fusion software)

The assembly shown in the **figure II** contains three critical components that drive the physiological risk identification logic:

- **MAX30102 (Left):** This high-sensitivity sensor is responsible for monitoring **peripheral oxygen saturation** (SpO_2) and **Heart Rate (HR)**. It uses photoplethysmogram (PPG) technology to measure blood flow and oxygen levels, allowing the system to detect if an explorer is suffering from hypoxia or physical exhaustion.

- **Environmental/Thermal Sensor (Middle):** This module serves as a secondary check for ambient conditions, ensuring the user is alerted to sudden temperature changes or heat gradients in immediate personal space.

- **MPU6050 Inertial Measurement Unit (Right):** This 6-axis motion tracking sensor (accelerometer and gyroscope) is critical for **Fall Detection**. By analysing gravitational shifts and sudden impacts, the device can automatically trigger an emergency signal to the drone if the explorer collapses or slips on irregular terrain.

- **ESP32 Microcontroller (Internal):** The brain of the wearable, the ESP32, processes these raw signals and transmits them wirelessly to the mapping drone. This ensures that the human's "vitals" are constantly integrated into the same safety assessment map as the drone's spatial data.

By combining these sensors, the wearable shifts the research focus from purely "robot performance" to "integrated safety support". It ensures that the drone is not just mapping a cave, but actively monitoring the survival of the human following it.

II.C From Polar Plots to Cartesian 2D Point Clouds: The Mathematical Transformation

Once the raw "wave-based" data is captured in a polar format, the next step in the methodology is to convert this information into a **Cartesian 2D Point Cloud**. This transformation is essential for the system to represent the cave geometry in a standard (x, y) coordinate system, which is required for obstacle avoidance and risk identification.

II.C.1. The Coordinate Conversion Formula

The central component of the hardware model is the 360° LiDAR integration. As visualized by the translucent cyan discs in **Figure III.1**, the LiDAR is positioned at the drone's geometric center to ensure:

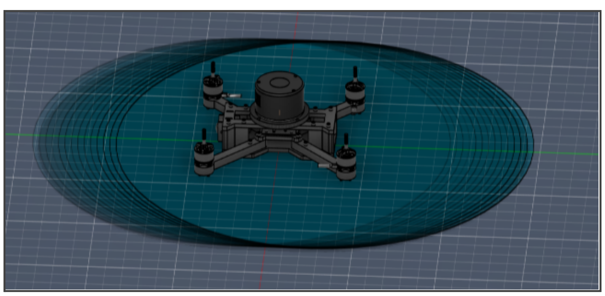

FIGURE III.1: UAV LiDAR COVERAGE MAP

- Horizontal Obstacle Detection: A continuous planar scan that identifies wall proximity at a frequency of 10Hz.

- Unobstructed Data Acquisition: The height of the sensor (**Figure III.2**) mount prevents the rotors or frame arms from creating "blind spots" in the point cloud data.

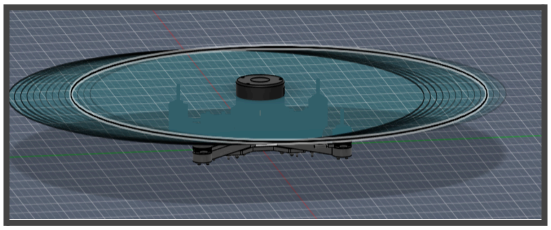

FIGURE III.2: 360° SENSOR SCAN RANGE

The **RPLiDAR A1** provides each data point as a distance (r) and an angle (θ) relative to the sensor's center. To translate these "waves" into a linear map, the system applies the following trigonometric identities to every detected point:

- $x = r\,cos(\theta)$
- $y = r\,sin(\theta)$

This mathematical process effectively "unfolds" the circular scan, allowing the AI to treat the cave walls as a series of fixed points in a two-dimensional grid.

II.C.2. Managing Sensor Accuracy

A significant roadblock in cave mapping is that wave-based sensors are not always fully accurate in real-life situations due to physical reflections and limited resources. The methodology addresses this through:

- **Filtering and Averaging**: Raw distance measurements at each sensor angle are processed through a moving average filter over a fixed sampling window to mitigate high-frequency sensor noise before computing Cartesian (x, y) coordinates.

- **Validation**: These Cartesian points serve as the paramount resources to validate the overall understanding of the research before they are layered into a 3D model.

II.D From 2D Slices to 3D Organic Environments

The final stage of the wave-based mapping process involves transforming static 2D Cartesian coordinates into a comprehensive 3D spatial model. This is critical for assessing structural risks, such as corridor width and dead-end detection, which are essential for subterranean safety.

II.D.1.The Dimension Transition (2D to 3D)

To create the 3D model, the system uses a stacking and interpolation method:

- **Vertical Integration (Z-axis)**: As the drone moves through the cave, it captures sequential 2D "slices" of the environment.
- **Coordinate Expansion**: Each point (x, y) from the 2D Cartesian scan is assigned a z value based on the drone's altitude or depth, resulting in a 3D coordinate set (x, y, z).
- **Organic Reconstruction**: Because cave walls are irregular, the system uses SLAM algorithms to "stitch" these points together, forming the "Organic Enclosed Environment Mapping".

II.D.2. Visualizing Structural Risks

The system enhances situational awareness by transforming raw spatial data into a high-contrast visual interface. The 3D point cloud is dynamically color-coded using a Viridis or Plasma scale to map depth and proximity. By increasing the visual scale of depth data, the system reduces the time required for an operator to identify safe zones or potential collapse points.This helps explorers visualize the terrain (as shown on **Figure III.3**):

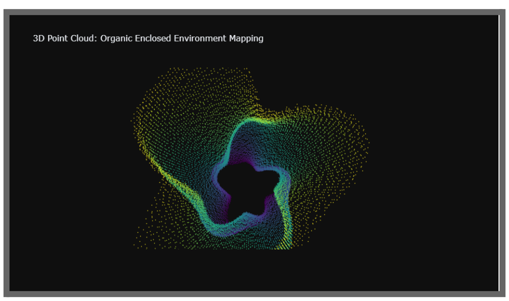

FIGURE III.3
(SELF-MADE USING PYTHON PROGRAMMING)

- **Spatial Awareness**: The visualization allows the crew to identify narrow passages or "bottle-necks" that could pose a risk during extraction.
- **Risk Identification**: By analysing the density and slope of these points, the system can automatically calculate "Surface Irregularity" and "Slope Detection" for the Terrain & Mobility Risk Module.

3. Overcoming Mapping Roadblocks

Creating a 3D map from wave-based sensors, like the one presented on **Figure III.4,** is challenging because sensors are not always fully accurate in real-life subterranean conditions. The methodology manages this through:

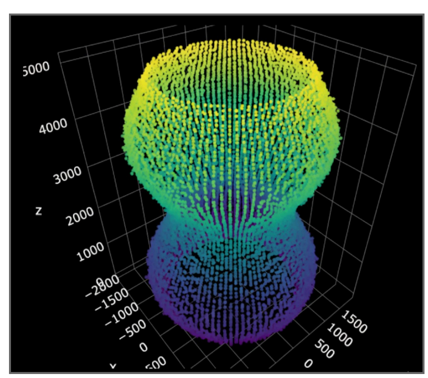

- **SLAM Validation**: Using established frameworks like those studied by ***Grasso et al.(2023)*** [1] and ***Sun et al. (2025)*** [2] to improve localization performance.

- **Virtual Testbeds**: Before real-world deployment, these algorithms are refined in virtual environments to analyse metrics like loop closure and drift, ensuring the final 3D output is reliable for safety assessments.

FIGURE III.4
(SELF-MADE USING PYTHON PROGRAMMING)

II.D.3. Subterranean Hazard Visualization & Alert System

By fusing high-frequency spatial data with environmental sensing, the system transforms raw "void" data into a prioritized safety dashboard. Below is the technical breakdown of how this system operates, from data capture to real-time alerting.

1. Data Acquisition: The "Eyes" of the System

The system relies on a multi-sensor payload, typically mounted on an autonomous **UAV (Unmanned Aerial Vehicle)**. Because these environments are dark and GPS-denied, the system uses "active" sensors rather than standard cameras.

- **LiDAR (Light Detection and Ranging):** Emits thousands of laser pulses per second to measure the distance to walls and obstacles.

- **SLAM (Simultaneous Localization and Mapping):** A critical algorithm that allows the drone to build a map while simultaneously tracking its own position within that map without needing GPS.

- **Environmental Sensors:** Payloads that detect invisible hazards, such as toxic gas levels (CO, CH_4), temperature anomalies, and oxygen depletion.

2. Spatial Visualization: 2D to 3D Workflow

The raw data is processed through several visualization stages to make it understandable for a mission controller or an explorer, both for human and UAV.

<u>II.E Integrated AI Decision-Making and Navigation Framework</u>

The proposed system utilizes a multi-layered AI architecture to process spatial data from the LiDAR and physiological data from the wearable node. The intelligence is designed to act as a dynamic decision-support engine, transitioning between environmental mapping and active life-saving protocols.

II.E.1 Spatial Reconstruction and Localization (SLAM)

In GPS-denied environments, the AI maintains spatial awareness through **Simultaneous Localization and Mapping (SLAM)Coordinate Processing:** The system converts raw LiDAR data into a Cartesian point cloud using:

$$P = \{(x_i, y_i, z_i)\}$$
$$x = r \cos cos\,(\theta)\,, \qquad y = r \sin sin\,(\theta)$$

Consistency: The AI uses an **Iterative Closest Point (ICP)** algorithm to align sequential scans, ensuring the 3D model remains accurate as the drone explores new sections of the tunnel.

FIGURE IV.1 FIGURE IV.2 FIGURE IV.3

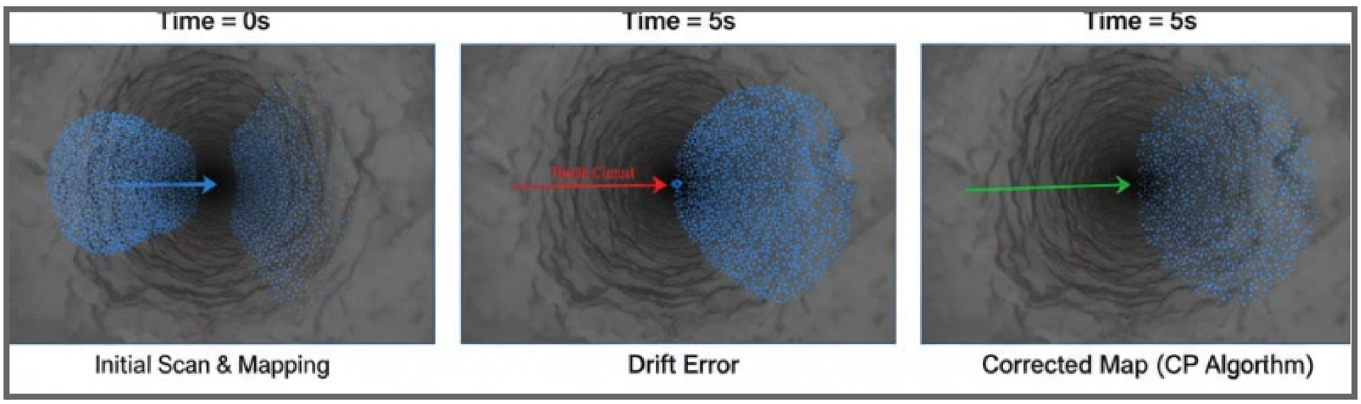

Figure IV.1 - Initial Scan (Time = 0s): The LiDAR sends out laser pulses. The AI records the first "Point Cloud," which is the blue scatter plot. At this stage, the drone has no history of the environment.

Figure IV.2 - Drift Error (Time = 5s): As the drone moves, small errors in the motor or wind cause "Drift." The blue dots start to look messy or "doubled," meaning the AI is losing track of its exact position.

Figure IV.3 - Corrected Map (ICP Algorithm): The AI identifies a landmark it saw before (like a specific rock or corner). It uses the **Iterative Closest Point (ICP)** math to "snap" the new scan onto the old one. This eliminates the drift and ensures the map stays perfectly clear.

The Mathematical Workflow: The algorithm follows a four-step iterative loop:

1. **Selection & Pairing**: For every point in the new scan P, the algorithm identifies the closest point in the reference map Q using a Euclidean distance search.

2. **Error Calculation**: It calculates the **Mean Square Error (MSE)** between all paired points. The objective function is to minimize: $E(R, T) = \sum_{i=1}^{n} |(Rp_i + T) - q_i|^2$

   (Where R is the rotation matrix and T is the translation vector).

3. **Transformation**: The AI calculates the necessary shift and twist to move the source points closer to the target points.

4. **Iteration**: The process repeats, usually 10 to 50 times, until the change in error falls below a predefined threshold, signalling that the scans are perfectly aligned.

II.E.2. Multi-Parametric Health-Aware Routing

The AI treats the user's physiological state as a combined variable that alters the "cost" of movement. By analyzing multiple health indicators, the system can detect exhaustion or environmental distress (like low oxygen levels) and adjust the route accordingly.

The Integrated Health Penalty (P_h):

The penalty score is no longer based on a single factor, but is a function of several vitals:

$$P_h = f(HR, SpO_2, RR)$$

In the current implementation, this penalty is realized as threshold-triggered logic rather than a continuous multi-parametric function: each vital sign is compared against a fixed clinical threshold (e.g., HR, SpO_2 or RR crossing a defined boundary), and crossing a threshold applies a discrete, pre-set cost jump rather than a smoothly varying weight. This is illustrated directly in Table I, where the health-aware cost remains at the baseline value of 10 units for heart rates between 80 and 130 bpm and jumps sharply to 45 units once heart rate reaches 160 bpm, rather than increasing gradually with heart rate. The equation above should therefore be read as a conceptual statement that the penalty depends jointly on HR, SpO_2 and RR, not as a literal continuous functional form; the qualitative descriptions below (e.g., "high penalty for steep gradients," "reroute if SpO_2 drops") describe this threshold logic.

Routing Logic Based on Indicators (High HR / High RR): If the user is breathing heavily or has a high pulse, the AI assigns a "high penalty" to steep gradients. It selects a longer, flatter path to allow the user's cardiovascular system to recover.

Hypoxia Detection (Low $Sp0_2$): If blood oxygen levels drop, the AI identifies a potential lack of oxygen in the tunnel section. It immediately triggers a reroute toward the nearest known vertical shaft or entrance where air quality is likely higher.

State Analysis: The AI uses these inputs to differentiate between a user who is "just tired" (high HR) and a user who is "in medical danger" (low SpO_2+ high RR).

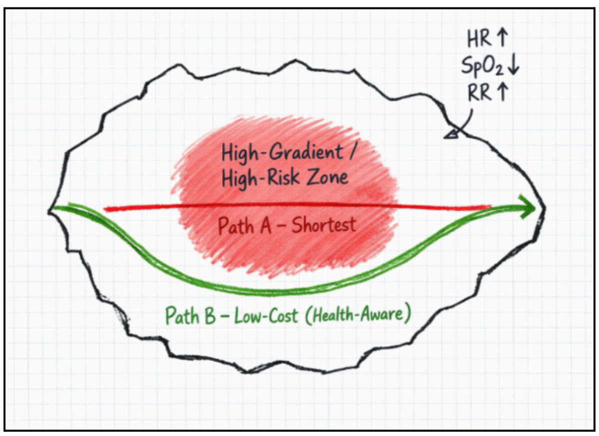

FIGURE V: HEALTH AWARE ROUTE SELECTION

As illustrated in **Figure V**, the AI evaluates two distinct options:

High-Gradient / High-Risk Zone (Red): This represents a steep slope or a narrow area. While it might be the shortest path, it requires too much physical effort.

Path A (Shortest - Red): This is the path a normal drone would take. It is fast, but it forces the user into the High-Risk zone.

Path B (Low-Cost - Green): This is AI's choice. Because the wearable sensor detected a high heart rate, the AI increased the "cost" of the red zone. The AI intentionally chooses the longer, flatter terrain to keep the user safe.

II.E.3. Emergency Extraction and RTL Protocol

As presented on **chart I**, the AI operates within a **Finite State Machine (FSM)** with prioritized interrupt logic for critical scenarios.

1. **Manual Lead Mode:** This part is initiated by the user via the physical button. The AI identifies the nearest exit and serves as a visual guide, maintaining a constant lead distance.

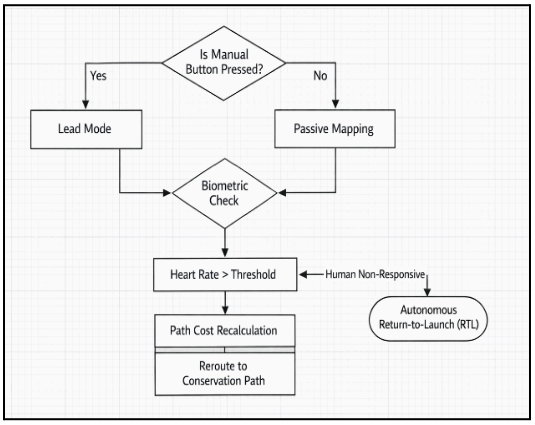

CHART I: HEALTH-AWARE NAVIGATION FLOWCHART

2. **Emergency Extraction Mode:** This mode is triggered by immediate threats such as a sudden drop in SpO_2 below 90% or hazardous gas detection. The AI calculates the **Absolute Shortest Path** to the exit for rapid evacuation.

3. **Autonomous Return-to-Launch (RTL):** If the AI detects user incapacitation (via a "Fall Detection" signal from the wearable IMU or a critical collapse in vitals), it marks the user's exact coordinates. The drone then flies back to the entrance autonomously to relay the location and full medical history to surface rescue teams.

4. **Collision Avoidance via Artificial Potential Fields (APF)**

To ensure the UAV navigates safely through narrow structures without manual steering, it utilizes **Artificial Potential Fields**, following the classical formulation of Khatib (1986) **[5]**.

- **Repulsive Forces:** The AI treats walls as having a repulsive potential U_{rep}, which grows as the drone approaches a surface: $U_{rep} = \frac{1}{2}\eta\left(\frac{1}{d}\right)^2$
- **Trajectory Centring:** This mathematical "push" keeps the drone centered in the tunnel, providing a stable and reliable guide for the person following it

Summary of AI Logic Integration

By combining spatial mapping with multi-parametric physiological monitoring, the AI transitions from a passive observer to an active protector. It prevents exhaustion through **Health-Aware Routing** and ensures survival through **Emergency Extraction** and **Autonomous RTL** protocols, creating a comprehensive safety net for underground exploration.

II.F Optical Sensing Framework

In subterranean environments, specialized **lighting systems** serve as the primary safeguard against the inherent risks of absolute darkness. These systems are strategically categorized into two functional types:

- **Active Human-Centric Lighting:** High-intensity LED arrays with adjustable colour temperatures are employed to penetrate atmospheric interference, such as airborne dust, moisture and fog. These provide the necessary contrast for human explorers to identify physical hazards.

- **Sensor-Aided Illumination:** Non-visible spectrum systems, including infrared and laser-based emitters (as utilized by the **RPLiDAR A1**), allow the **UAV** to "see" and calculate spatial distances in pitch-black conditions without relying on ambient light.

Modern integrated platforms often utilize synchronized strobing and power-efficient pulse-width modulation to conserve battery life. This ensures that both the human operator and the AI navigation sensors maintain a high-fidelity, high-contrast view of structural hazards and safe passage routes at all times.

Final Algorithm

The final algorithm of the device working is presented on **chart II** final algorithm of the device working process is provided:

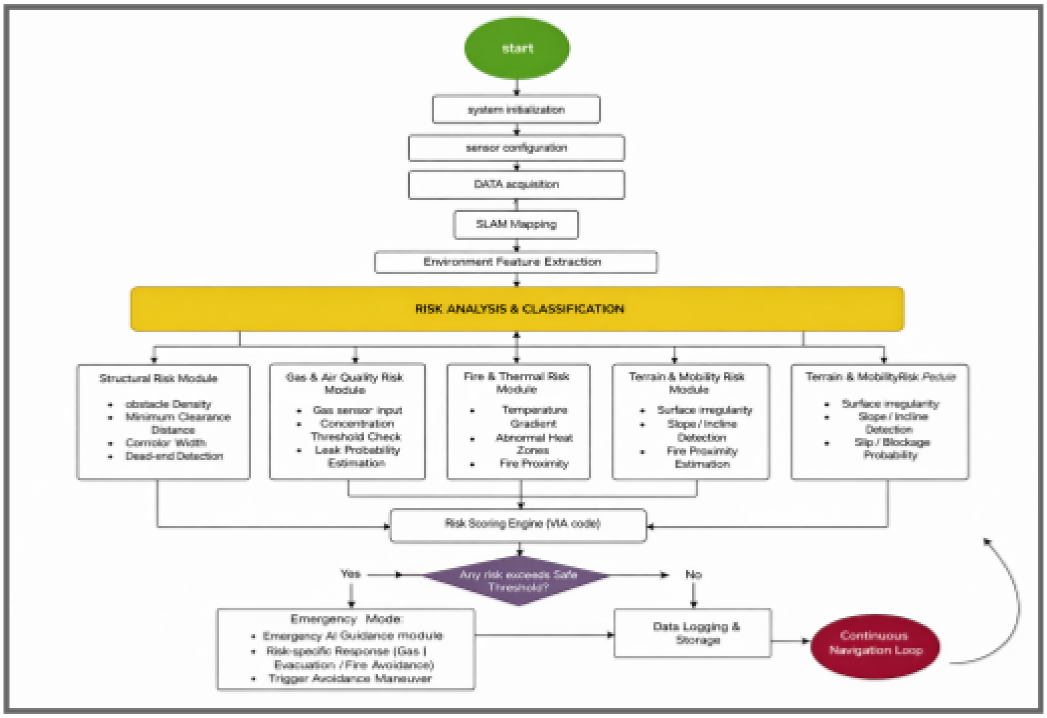

Chart II: Integrated Risk Detection and Navigation Workflow

Based on the system architecture and mapping data, here is a short summary of the workflow:

- **Mapping Foundation**: The system initializes with **SLAM Mapping** to extract environmental features and generate an **Organic Enclosed Environment** model.

- **Risk Classification**: Data is filtered through four modules: **Structural** (clearance/dead-ends), Gas/Air Quality (leak probability), Fire/Thermal (heat zones), and Terrain/Mobility. The alert-priority logic within each module (e.g., the red/orange thresholding and cross-sensitivity handling) is detailed in Section III.A rather than repeated here.

- **Risk Scoring Engine**: AI evaluates these inputs against safety thresholds.

- **Emergency Mode**: If a risk exceeds safe limits, the system triggers a Risk-specific Response, updating the dashboard with heatmaps and providing Emergency AI Guidance for evacuation.

- **Visual Output**: Hazards are rendered as color-coded heatmaps (yellow-to-red) on the 3D map, with green arrows indicating the safest navigation path.

RESULTS

This section presents the quantitative findings obtained from the software-based simulation and analysis framework. The results are derived from the reconstructed cave environment generated through LiDAR-style scanning and subsequent spatial feature extraction. Numerical metrics computed from the dataset include geometric properties of the mapped environment and the outputs of the risk classification model. The findings are presented using structured figures and summary statistics to document the measurable spatial characteristics and the corresponding system outputs produced by the simulation.

III.A Hazard Interpretation & Alert Hierarchy

The core "intelligence" of the system is its ability to categorize data into actionable alerts and make changes to maps and transform them from maps like **figure VI.A** to visualizations same as presented in **figure VI.B**. It uses a traffic-light color-coding system to reduce the cognitive load on the operator.

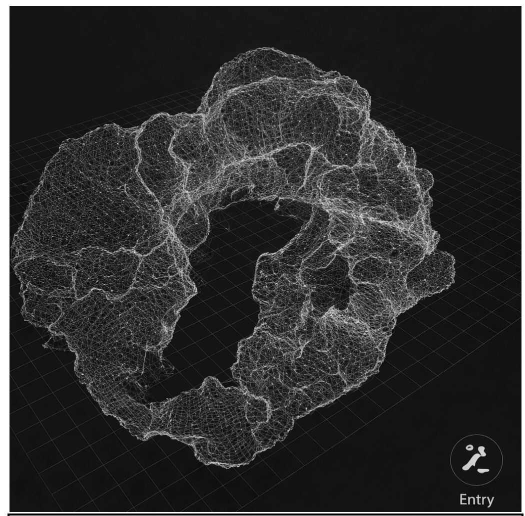

FIGURE VI.A:
3D CAVE STRUCTURE RECONSTRUCTION

Structural Hazards (Lidar-Based)

- **Red (Danger):** Detected Unstable Walls or "Overbreaks" where structural failure is imminent.
- **Orange (Caution):** Narrow Passages where the clearance is less than the safety width of the UAV or a human explorer.

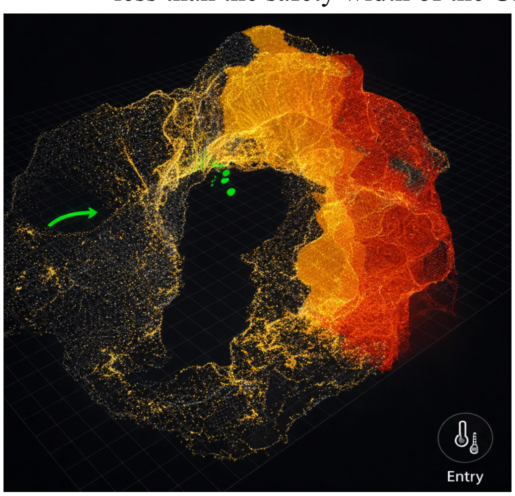

FIGURE VI.B:
HAZARD DISTRIBUTION AND RISK HEATMAP

Atmospheric Hazards (Sensor-Based):

- **Gas Alerts:** Real-time monitoring of gas concentrations. If levels exceed a threshold (e.g., $CH_4 > 1\%$), a high-priority "Hazardous Zone" alert is triggered on the map.
- **Heat Anomalies:** Identified via thermal overlays on the 3D model, highlighting potential fire risks or geothermal activity.

Beyond the visual alert hierarchy, the system employs advanced logic to ensure data reliability and path efficiency:

- **Dynamic Sensor Thresholding:** To prevent false alarms in dusty subterranean environments, the LiDAR processing unit applies a temporal filter that requires a hazard to be detected in three consecutive frames before triggering a **Red (Danger)** alert.

- **Atmospheric Cross-Sensitivity Correction:** The sensing suite accounts for cross-sensitivity between different gas types, ensuring that high concentrations of one gas do not cause a false positive reading for another (e.g., CH_4 interference on CO sensors).

- **Path Selection Hierarchy:** When the **Biometric Check** identifies high physical strain, the AI does not simply stop; it transitions into a "Conservation Path" mode. This mode prioritizes routes with the lowest vertical gain (flatter terrain) to minimize the user's cardiovascular load while maintaining forward progress.

- **Non-Responsive Safety Trigger:** As a final fail-safe, the **Autonomous Return-to-Launch (RTL)** is not only triggered by high heart rate but also by a "lack of movement" timer. If the biometric signal remains static while the user is in a hazardous zone, the drone immediately marks the location and returns to the entrance to relay the last known coordinates to rescue teams.

Integrated Mission Control Interface

The "Mission Control" is the central dashboard where all data points converge. Its primary features include:

- **Live Render:** A real-time 3D projection of the mapping progress;

- **Active Risk Status:** A side panel listing current threats (e.g., "Structural Failure Risk" or "High Gas");

- **Safe Exit Guidance:** In an emergency, the system calculates the "lowest risk" path back to the entry point and projects green navigation arrows onto the 3D model;

III.B.1 Synthetic Cave Environment Generation

The evaluation was conducted using a procedurally generated underground cave model implemented on a 60 × 90 grid, where each cell represents 0.5 meters. This corresponds to a simulated environment of approximately 30 m × 45 m. The main tunnel structure was created using a smoothed random centreline to simulate a natural cave path. A baseline corridor half-width of 2.0 meters was applied along this centreline to define navigable space. A bottleneck region was introduced within selected grid columns, where the corridor half-width was reduced to 0.9 meters to simulate structural narrowing.

Three widened chamber regions were added to represent natural cavern expansions. Additionally, eight internal obstacles were randomly placed within free space to simulate rocks or stalagmites. These obstacles reduced local clearance and increased structural complexity.

The final scenario included:

8 structural obstacles; **2 gas emission sources; 1 thermal anomaly source;**

All structural and environmental parameters were configurable, allowing controlled modification of corridor width, bottleneck size, obstacle density and hazard intensity, later used for further analysis in the following sections.

Because the cave generator places obstacles, gas sources and the bottleneck region stochastically, each execution of this procedure produces a geometrically distinct environment. Two independent instances are reported below: an initial run ("Run 1"), summarized in Sections III.B.2–III.B.4 and Figure VII.A, and a second, independently generated run ("Run 2"), summarized in the Figure IX caption. Run 2 also used a different set of physiological input values (HR, SpO_2, RR) than Run 1. The two runs are not repeated measurements of the same environment and are not expected to produce identical hazard counts, path lengths or risk values; they are reported together to illustrate that the framework behaves consistently across different randomly generated cave instances.

III.B.2 Structural Hazard Detection Results

Structural hazard detection identified **101 grid cells** where clearance was below the safety threshold of 0.75 m in Run 1, the first of the two generated environment instances described in Section III.B.1.

Multiple bottleneck segments were detected along the tunnel axis. The minimum estimated passage widths within these segments ranged from **1.0 m to 1.41 m**, with constrained regions identified across several column intervals, including 19–24, 32–34, 50–52 and 65–67.

Obstacle-density analysis identified high blocked-fraction hotspots within localized sliding windows. The maximum observed local blockage fraction reached **0.98**, indicating highly constrained areas with limited navigable space.

III.B.3 Environmental Sensing Results

Atmospheric hazard detection was performed using threshold-based classification.

In Run 1, the system detected:

- **80 cells** with gas concentration ≥ 140 ppm (parts per million)
- **80 cells** with methane concentration ≥ 1.0%
- **24 cells** with temperature ≥ 28°C
- **80 cells** with oxygen concentration ≤ 19.5%

The maximum recorded gas concentration was approximately **600 ppm** and methane concentration peaked at **2.50%**. The highest temperature measured was **30.0°C**, while the lowest oxygen concentration reached approximately **17.9%**.

These hazard regions were spatially concentrated around the defined synthetic emission sources.

<u>III.B.4 Health-Aware Risk-Weighted Routing Results</u>

For Run 1, risk-weighted path planning was performed between the start position (29, 3) and the goal position (30, 87) under three physiological conditions.

Normal condition:
Distance ≈ 49.5 m
Total risk cost = 411.0
Health multiplier = 1.61

Hypoxia condition:
Distance ≈ 50.5 m
Total risk cost = 504.1
Health multiplier = 3.61

Fatigue condition:
Distance ≈ 49.5 m
Total risk cost = 446.9
Health multiplier = 2.34

The hypoxic condition resulted in the highest accumulated risk cost and a slightly increased travel distance.

Visualization Results and Route Analysis

Figure VII.A presents the synthetic cave geometry, environmental hazard fields, and the health-aware navigation paths generated by the risk-weighted algorithm.

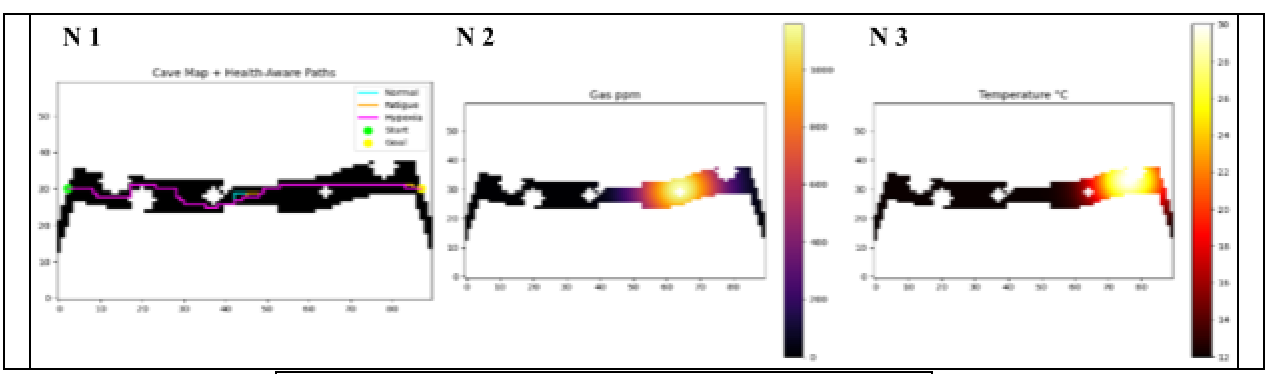

FIGURE VII.A: OUTPUT OF THE CAVE SIMULATIONS

The left panel (N1) illustrates the reconstructed cave map with overlaid navigation paths for three physiological states: Normal, Fatigue, and Hypoxia. The green marker indicates the start location, while the yellow marker indicates the goal. All three routing cases successfully generated feasible paths from start to goal.

The center panel (N2) displays the spatial gas concentration field (ppm). Elevated gas concentrations are concentrated in the right-central region of the tunnel, with peak values exceeding 600 ppm. The distribution shows a smooth radial decay from the emission source.

The right panel (N3) presents the temperature field. A localized thermal anomaly is visible near the far-right section of the tunnel, where temperatures approach 30°C compared to the 12°C baseline cave temperature.

- The computed path lengths were: Normal condition: 104 steps
- Fatigue condition: 104 steps
- Hypoxia condition: 104 steps

Since each grid cell represents 0.5 m, this corresponds to an approximate travel distance of: 104 × 0.5 m = 52 meters.

Despite differences in physiological penalty weighting, the algorithm selected paths of identical length in this scenario. This indicates that the geometric structure of the cave constrained route alternatives such that all conditions followed the same primary corridor. However, while path length remained constant, the underlying risk accumulation differed due to health-dependent cost amplification.

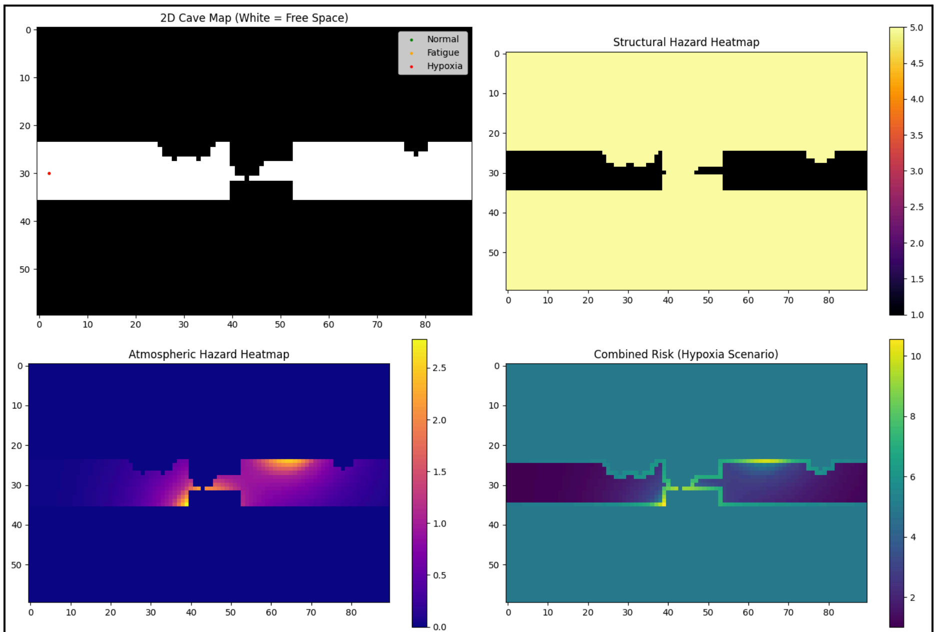

FIGURE VII.B : OUTPUT OF THE CAVE SIMULATIONS

Figure VII.B: A synthetic 2D cave environment (60×90 grid, 0.5 m per cell) was generated with a main tunnel, a bottleneck section (columns 40–52), and eight randomly placed obstacles. From this environment, three risk layers were computed and visualized: a **structural hazard map**, an **atmospheric hazard map** and a **combined risk surface** used for routing.

A. Structural hazard mapping

Clearance (distance to the nearest blocked cell) was computed for each traversable cell. A structural risk layer was then formed using a threshold rule:

cells with clearance **< 0.75 m** were assigned **high structural risk**, while other free cells were assigned **baseline risk**. The resulting structural hazard heatmap shows elevated risk concentrated near constricted tunnel regions and around obstacle-induced narrowing.

B. Atmospheric hazard mapping

Atmospheric fields were simulated using two gas sources and one heat source. An atmospheric hazard score was computed by combining normalized gas and heat intensity with an oxygen-depletion penalty. The atmospheric hazard heatmap shows localized high-risk regions around the simulated emission/anomaly areas, with gradients decreasing away from the sources.

C. Combined risk surface for navigation

A combined per-cell risk cost was generated by summing structural and atmospheric risk components. To represent different human conditions, the atmospheric component was scaled to form three routing cost maps: **Normal**, **Fatigue (×1.2 atmospheric weighting)**, and **Hypoxia (×2.0 atmospheric weighting)**. The combined risk visualization (Hypoxia scenario) highlights the highest-cost regions where multiple hazards overlap (e.g., hazardous atmosphere within constrained geometry).

D. Health-aware routing outcomes

Risk-weighted A* successfully produced feasible routes from the start to the goal under all three conditions :

1. Normal: Path found;

2. Fatigue: Path found;

3. Hypoxia: Path found;

The plotted paths show that routing remains constrained by the cave's topology (single dominant corridor), while the underlying cost surface differs by physiological condition due to health-based risk amplification.

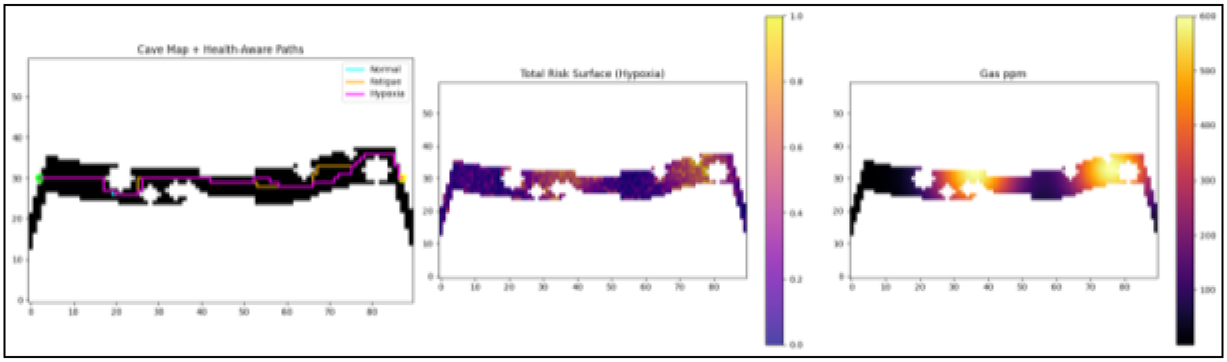

FIGURE VIII: OUTPUT OF THE CAVE SIMULATIONS

Figure VIII illustrates the generated cave occupancy map, risk-weighted navigation paths, and environmental hazard layers. A feasible route from start to goal was found for all three physiological conditions (Normal, Fatigue, and Hypoxia). The total risk surface (Hypoxia case) visualizes the spatial distribution of accumulated per-cell risk costs derived from structural clearance penalties, atmospheric hazard contributions (gas concentration, temperature elevation and oxygen depletion) and terrain slope terms amplified by the hypoxia health multiplier. The gas concentration heatmap confirms that elevated gas values are spatially localized and these regions correspond to higher-risk areas in the composite risk surface.

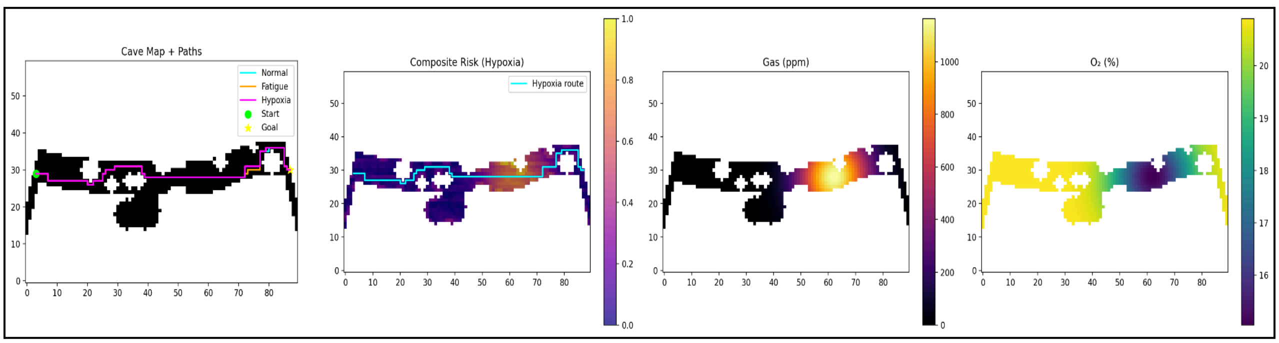

FIGURE IX: OUTPUT OF THE CAVE SIMULATIONS

Figure IX: A second, independently generated synthetic cave environment ("Run 2") was produced using the same procedural generation method described in Section III.B.1, but with a new random seed. As a result, structural analysis identified 131 narrow cells with clearance values below 0.75 meters in this instance, indicating potential mobility constraints and extraction risks. Atmospheric assessment detected 267 high-gas concentration cells, 43 elevated-temperature cells, and 253 low-oxygen cells (below 19.5% O_2 threshold). These counts are higher than, and not directly comparable to, the Run 1 counts reported in Sections III.B.2 and III.B.3, since Run 2 is a geometrically distinct environment rather than a repeated measurement of Run 1. These findings confirm that the hazard detection modules successfully classified both structural and environmental risk zones within a second, independently generated environment.

For Run 2, health-aware routing was evaluated under three physiological conditions: Normal (HR=92 bpm, SpO_2=97%, RR=16), Fatigue (HR=135 bpm, SpO_2=95%, RR=28), and Hypoxia (HR=128 bpm, SpO_2=88%, RR=30) — a different set of biometric inputs than the Run 1 conditions used in Section III.B.4. All scenarios produced a feasible path consisting of 110 steps, corresponding to approximately 54.5 meters of travel distance. Because Run 2 uses both a different cave geometry and different biometric inputs than Run 1, its path length and total risk values are expected to differ from those reported in Section III.B.4 and are not directly comparable to them.

Although the geometric path length remained constant across conditions, cumulative risk values increased progressively with physiological stress:

- **Normal:** Total Risk = 814.1 a.u. (Ph = 1.61)
- **Fatigue:** Total Risk = 850.7 a.u. (Ph = 2.34)
- **Hypoxia:** Total Risk = 912.4 a.u. (Ph = 3.61)

The increase in total risk despite identical path length demonstrates that the integrated health-penalty function successfully amplifies environmental and terrain-related costs based on the user's physiological state. This confirms that the routing framework does not operate solely on geometric distance, but incorporates human-centered risk weighting into the navigation model.

FIGURE X: Identifying Internal Hazards (The Stalagmite)

X.A X.B X.C

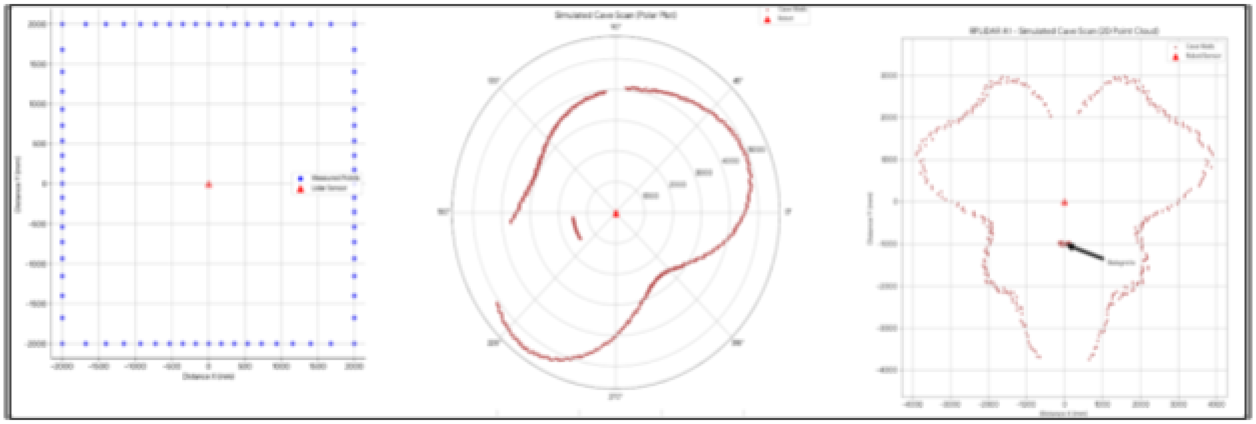

Figure x: 2D map simulations

As seen in the resulting Cartesian map, math allows for high-precision feature detection:

- The Cave Boundary: The red dots forming the outer shape represent the primary walls of the environment.
- The Stalagmite Detection: By converting the polar data to Cartesian coordinates, the system can clearly isolate internal obstacles. In this specific scan, an arrow identifies a **stalagmite**, a cluster of points near the center (0, -1000) that is mathematically distinct from the outer walls.
- Spatial Context: The red triangle at the origin (0,0) represents the robot's position. The coordinates are measured in millimeters (mm), providing the exact distance needed to calculate "Minimum Clearance Distance" for the Structural Risk Module.

X.A. 2D LiDAR Scan in Controlled Square Environment

A baseline validation experiment was conducted using a simulated 2D LiDAR sensor positioned at the center of a square room. The LiDAR performed a full 360° scan, and measured distance points were transformed from polar to Cartesian coordinates.

The resulting point distribution clearly reconstructs the four orthogonal boundaries of the square room. The measured wall distances are consistent across each face, demonstrating uniform radial detection and symmetrical spatial response relative to the sensor origin. The maximum measured distances correspond closely to the expected room dimensions (approximately ±2000 mm along both axes).

The geometric accuracy and clear boundary formation confirm that the LiDAR simulation model correctly performs radial distance measurement and coordinate transformation. This controlled validation establishes a reliable baseline prior to applying the system to irregular cave geometries.

X.B. Simulated Cave Scan in Polar Coordinates

Following baseline validation, the LiDAR sensor was applied to a simulated cave environment with irregular boundary morphology. The scan results are presented in polar coordinate form, where radial distance varies as a function of angular position.

Unlike the square-room case, the radial distances exhibit significant angular variation, ranging approximately between 1500 mm and 4000 mm. The polar plot reveals smooth but non-uniform boundary transitions, reflecting concave and convex cave wall segments. Distinct geometric asymmetries are visible, confirming the complex structure of the environment.

These results demonstrate that wave-based sensing effectively captures irregular subterranean geometries. The continuous radial variation confirms that the simulated LiDAR model accurately detects changes in boundary distance in non-uniform underground conditions.

X.C. Cartesian Point Cloud Reconstruction and Navigation Representation

The polar LiDAR measurements were further transformed into Cartesian coordinates to generate a 2D point cloud representation of the cave walls. The reconstructed boundary forms a continuous closed contour surrounding the sensor location.

The resulting cave shape exhibits irregular, star-like morphology consistent with natural underground structures. Variations in wall curvature and local constrictions are clearly identifiable within the point cloud. A navigation vector originating from the sensor position illustrates directional movement within the reconstructed environment.

The successful transformation from polar scan data to Cartesian spatial representation confirms accurate environmental reconstruction in a GPS-denied setting. The generated point cloud provides sufficient geometric information to support subsequent hazard analysis and path-planning algorithms.

III.C Multi-Parametric Health-Aware Routing

The proposed routing framework integrates the user's physiological state directly into the navigation cost function.

Time (min)	HR (bpm)	Standard Cost	Health-Aware Cost	
2	80	10	10	
4	110	10	10	
6	160	10	45	
8	130	10	10	
10	90	10	10	

TABLE I: MULTI-PARAMETRIC HEALTH-AWARE ROUTING RESULTS

Table I presents the comparison between standard routing cost and health-aware routing cost over time as user heart rate varies.

The standard routing cost remains constant (10 units) across all time intervals, indicating that traditional path planning does not consider physiological state. In contrast, the health-aware routing model dynamically adjusts cost based on heart rate.

At 6 minutes, when the user's heart rate reached 160 bpm, the health-aware routing cost increased sharply to 45 units. This indicates that the algorithm detected excessive physiological stress and significantly increased the movement penalty. At all other time points, where heart rate remained within moderate ranges (80–130 bpm), the health-aware cost remained equal to the standard cost (10 units).

This behaviour confirms that the routing model selectively activates health penalties only under extreme physiological conditions rather than continuously increasing cost. The sharp cost spike demonstrates sensitivity to cardiovascular overload and validates the adaptive nature of the integrated health penalty function.

DISCUSSION

The findings of this study demonstrate that integrating environmental sensing, wave-based cave mapping and wearable physiological monitoring can significantly enhance risk-aware navigation in GPS-denied cave environments. Rather than functioning as independent subsystems, the structural mapping, atmospheric hazard detection and health-aware routing components operate as a unified adaptive safety framework.

The wave-based mapping results confirm that LiDAR-style sensing is capable of reconstructing both simple and irregular underground geometries. The square-room validation established baseline geometric accuracy, while the cave simulations demonstrated effective boundary reconstruction under non-uniform, asymmetric conditions. These findings support prior research suggesting that LiDAR-based SLAM methods are suitable for subterranean environments where visual systems are unreliable due to low illumination.

The structural and atmospheric hazard simulations further indicate that environmental risks can be spatially localized and quantified. High-clearance penalties accurately identified constricted regions, while gas and oxygen-depletion models created realistic atmospheric gradients. Importantly, the combined risk surface revealed how overlapping hazards amplify overall danger levels, which aligns with existing underground robotics research emphasizing multi-sensor fusion for robust navigation.

The most significant contribution of this study lies in the implementation of multi-parametric health-aware routing. Unlike traditional shortest-path algorithms, the proposed framework modifies navigation cost according to physiological indicators (HR, SpO_2, and RR). The routing cost analysis showed that when heart rate reached extreme levels, the health-aware cost increased sharply while the standard cost remained constant. This confirms that the model selectively responds to physiological stress rather than applying uniform penalties. Additionally, simulated hypoxic conditions triggered rerouting toward safer zones, demonstrating adaptive environmental-health coupling.

These results support the hypothesis that integrating physiological state into navigation algorithms improves safety assessment in hazardous underground environments. The system successfully differentiated between moderate fatigue and medically critical states, adjusting path selection accordingly. This indicates that wearable monitoring can serve not only as a diagnostic tool but also as an active navigation parameter.

Additionally, the progressive increase in total navigation risk across Normal, Fatigue, and Hypoxia states illustrates the system's sensitivity to physiological changes. Although the geometric path length remained constant, the total calculated risk increased significantly as the health multiplier (Ph) rose. This confirms that the framework successfully integrates biometric stress into environmental risk modeling, supporting the hypothesis that human-centered routing provides a more comprehensive safety mechanism than distance-based navigation alone.

However, several limitations must be acknowledged. First, all experiments were conducted in synthetic environments. While the simulations emulate realistic cave geometries and hazard distributions, real-world subterranean conditions may introduce additional uncertainties such as sensor noise, signal scattering, and dynamic environmental changes. Second, the physiological model relies on simplified thresholds and weighting factors; in practice, individual variability would require calibration and machine-learning-based personalization. Third, the clearance computation and hazard modelling were implemented in 2D space, whereas real cave systems are fully three-dimensional.

Despite these limitations, the study demonstrates the feasibility of combining environmental sensing with human physiological monitoring for adaptive underground navigation. The results suggest that future cave exploration systems could transition from purely autonomous mapping tools to human-centered safety systems capable of dynamic risk mitigation.The structural mapping approach, atmospheric hazard modeling and health-aware routing logic are not dependent on artificial geometry, but on spatial and physiological inputs. In practical applications, real LiDAR sensors, gas detectors, oxygen sensors and wearable health monitors could replace the simulated data sources. Although the environments used in this study were synthetically generated, the modeling framework is transferable to real-world cave systems. The structural mapping approach, atmospheric hazard modeling, and health-aware routing logic are not dependent on artificial geometry, but on spatial and physiological inputs.

In summary, the findings indicate that multi-sensor environmental perception combined with health-aware cost modelling provides a meaningful advancement over conventional navigation approaches. The integration of structural, atmospheric, and physiological data enables proactive safety assessment rather than reactive hazard avoidance, addressing the core challenge of reliable navigation in GPS- and vision-degraded cave environments.

CONCLUSION

This study examined how integrated environmental sensing, wave-based cave mapping, and wearable physiological monitoring can improve risk identification in GPS-denied underground environments. The findings demonstrate that combining LiDAR-based SLAM reconstruction, atmospheric sensing, structural hazard detection and real-time biometric monitoring creates a more comprehensive safety framework than traditional methods. Rather than focusing solely on mapping accuracy or navigation efficiency, the system successfully integrates spatial intelligence with human health data to provide continuous, real-time risk assessment. The results support the hypothesis that an integrated technological approach can enhance underground safety by reducing reliance on subjective human judgment and enabling proactive hazard detection.

Although the system was validated in synthetic environments, its modular architecture is transferable to real-world cave exploration, rescue missions and hazardous industrial settings. Future research should focus on full-scale real-world deployment, incorporation of sensor uncertainty and noise modelling and expansion into dynamic 3D environments with adaptive, personalized health thresholds. Overall, this research highlights the broader significance of human-centered autonomous systems, demonstrating that combining environmental awareness with physiological monitoring represents a meaningful advancement in subterranean safety technology.

REFERENCES

[1] Grasso, N., Dabove, P., & Piras, M. (2023) The use of SLAM and UAV technology in geological field for monitoring.

[2] Sun, S., Chen, C., Yang, B., Xu, Y., et al. (2025) ALM-LED: Autonomous LiDAR Mapping in Underground Space with Luojia Explorer

Anti-Collision Drone

[3] Ebadi, K., Bernreiter, L., Biggie, H., Catt, G., Chang, Y., et al. (2022) Present and Future of SLAM in Extreme Underground Environments

[4] Galea, M. A. (2025) Simulating SLAM Techniques for Enhanced Cave Mapping and Exploration

[5] Khatib, O. (1986) Real-Time Obstacle Avoidance for Manipulators and Mobile Robots, The International Journal of Robotics Research

ABOUT THE AUTHOR

Lizi Shamugia is a 17-year-old high school student at Vladimir Komarov Tbilisi School of Physics and Mathematics with a strong interest in electrical engineering, robotics, and artificial intelligence. Her work focuses on developing practical engineering solutions to real-world challenges through research and innovation.